General treatment of off-specular resonant soft x-ray magnetic scattering using the distorted-wave Born approximation: Numerical algorithm and experimental studies with hybrid chiral domain structures

Samuel Flewett,[1,*] Erick Burgos-Parra,[2,3] Mackarena Garrido Strelow,[1] Yanis Sassi,[3] Cyril Léveillé,[2] Fernando Ajejas,[3] Nicolas Reyren,[3] and Nicolas Jaouen[2]

[1]*Pontificia Universidad Católica de Valparaíso, Avenida Universidad 330, Valparaíso, Chile*

[2]*Synchrotron SOLEIL, Saint-Aubin, Boite Postale 48, 91192 Gif-sur-Yvette Cedex, France*

[3]*Unité Mixte de Physique, CNRS, Thales, Université Paris-Saclay, 91767 Palaiseau, France*

(Received 20 January 2021; revised 12 April 2021; accepted 13 April 2021; published 3 May 2021)

We present a numerical algorithm for the simulation of resonant x-ray magnetic scattering in reflection geometry for an arbitrary three-dimensional magnetization distribution over a multilayer sample utilizing the distorted-wave Born approximation. Our approach takes the medium boundary matrix approach for specular reflection, and the Born approximation typically used for off-specular reflection, combines the two, and adds the contribution from transmission through the sample before and after a reflection event. The algorithm is then tested on experimental data from an Al_2O_3/Co/Pt multilayer sample with hybrid Néel/Bloch/Néel domain walls at incidence angles at and near multilayer Bragg angles, and photon energies near the Co L_3 absorption edge, achieving high levels of agreement with experimental data. Incorporating the transmission components into the algorithm was found to explain the dichroism observed in scattering from Bloch-type domain walls, and uncovered the likely importance of diffuse scattering in transmission from the polycrystalline grain walls along the optical path of the x rays in the sample—a theme which deserves further investigation.

DOI: 10.1103/PhysRevB.103.184401

I. INTRODUCTION

A. General background

Over the past 20 years, the field of resonant elastic soft x-ray scattering has widely expanded into a standard tool for the nanometer-resolution characterization of magnetic domains in thin-film samples [1–8]. However, an important gap in the literature is the lack of a standard protocol for the modeling of resonant scattering, which has limited the degree to which quantitative conclusions may be extracted from experimental data. In this article, we begin by reviewing the theory literature on the topic, and then present our numerical implementation of the framework of Zak *et al.* [9–12] applied to a film whose magnetization varies not only in the out-of-plane direction but also in the plane of the sample. Our implementation allows the matrix formalism of Zak *et al.* [9–12] to be readily applied in three dimensions over a multilayer sample with inhomogeneous magnetization by making use of the distorted-wave Born approximation (DWBA) in reflection geometry. Here, we calculate the reflection coefficients for each numerical pixel in a "pancake stack" of imperfect reflecting surfaces (corresponding to each interface in a multilayer sample) and propagate the beam through the sample before and after each reflection event in order to account for differences in the absorption and phase shifts due to components of the magnetization parallel to the beam direction.

This research field can be said to have begun with the seminal publication by Dürr *et al.* in 1999 [2], when the characteristic asymmetric scattering pattern was first experimentally demonstrated with soft x rays for a stripe domain sample. This asymmetry when illuminated with circularly polarized x rays is due to the interplay between the σ-π and π-σ polarization shifting reflection from parts of the sample magnetized parallel to the scattering plane, and the π-π reflection from those parts magnetized perpendicular to the scattering plane. These magnetization-dependent changes in polarization on reflection are known as the magneto-optic Kerr effect (MOKE). A further development of the work by Dürr *et al.*, especially in terms of modeling, may be found in the work of Beutier *et al.* [3]. In their work, they also started from micromagnetic simulations, which are typically performed using software packages such as OOMMF [13] or MUMAX [14]. They start from the atomic level, defining the atomic scattering factors for the resonant soft x-ray interaction of elemental species s as derived from quantum mechanics [1]:

$$f_s = (\boldsymbol{e}\cdot\boldsymbol{e}')f_c^s + i(\boldsymbol{e}\times\boldsymbol{e}')\cdot\boldsymbol{M}^s f_{m1}^s + (\boldsymbol{M}^s\cdot\boldsymbol{e}')(\boldsymbol{M}^s\cdot\boldsymbol{e})f_{m2}^s, \tag{1}$$

where $\boldsymbol{e}$ is the incoming electric field vector; $\boldsymbol{e}'$ the rotated outgoing electric field vector; $\boldsymbol{M}^s$ the sample magnetization vector normalized to unity; and f_c^s, f_{m1}^s, and f_{m2}^s the charge, circular dichroic, and linear dichroic resonant scattering factors, respectively. For the 3d transition metals which will be dealt with in this paper, only the factors f_c^s and f_{m1}^s have

*samuel.flewett@pucv.cl

appreciable values. This is not universally the case, however, and the f^s_{m2} term needs to be taken into account for example in the case of the multiferroics of Ref. [15]. From these values of the atomic scattering factors, the authors of Ref. [3] calculated the scattering factor of each micromagnetic simulation cell by computing the sum of the atomic scattering factors over each cell, assuming constant magnetization across each cell. In turn, they summed each of these cell scattering factors over the the entire magnetic stripe domain period. This Born approximation (BA) formalism is similar to that used in crystallography, and accurately predicts the asymmetric diffraction which is a signature of stripe domain reflectometry with resonantly tuned soft x rays. More recent work with soft x rays using similar analysis procedures includes that of Fin *et al.* [16], where linearly polarized light was used to study buried domain wall structure in stripe domain samples, the work of Chauleau *et al.* [4] using circularly polarized light to study worm domain samples, and the study of the internal domain wall structure of skyrmion hosting compounds by Legrand *et al.* [17]. Zhang *et al.* [18] used resonant x-ray magnetic scattering (RXMS) to probe the three-dimensional (3D) structure of a skyrmion array, using atomic transition probabilities to calculate the absorption length and thus the relative weighting of the contributions from each layer within the sample. By invoking an exponential attenuation, Zhang *et al.* [18] and also Li *et al.* [19] are in effect employing the idea of the DWBA, an idea that is key to this present work. The chirality of a skyrmion array has also been characterized using RXMS, using the orientation of the observed asymmetric pattern as a probe of whether the domain walls are of Bloch, Néel, or some intermediate state [20]. Resonant scattering was also performed on a patterned NiFe (permalloy) sample by Diaz *et al.* [21], again utilizing the sum of the scattering factors as the tool for modeling the observed scattering behavior.

This paper deals with the forward problem of simulating an x-ray scattering pattern given an arbitrary 3D magnetization distribution in a multilayer sample and demonstrates the validity of the formalism with experimental examples. Compared with previously cited references where the BA is used, an important advantage of our method is the ability to include the effect of transmission on the resulting reflection scattering pattern. This is especially important where scattering is performed along Bloch walls with an extended line of interaction between the photons and the sample before and after the reflection event. Differential transmission along the Bloch walls will be shown here to result in a further dichroism additional to the classic asymmetry, a feature which is being exploited by Burgos-Parra *et al.* [22] to study the evolution of both Bloch and Néel domain walls under external field.

The algorithm presented in this paper was developed and improved through the task of analyzing experimental data. Some of these results have already been published [23], and others will be soon submitted for publication [22,24]. It is also an extension of previous work in transmission geometry [6,25]. The experimental material included was specifically chosen to test certain hypotheses which arose from the analysis of the data undergoing peer review [22], namely, the possibility of determining the depth of the Bloch part of the domain wall. Determining this depth has already been qualitatively explored by Zhang *et al.* [26] and is particularly interesting because it is believed to be related to the value of the Dzyaloshinskii-Moriya interaction (DMI) [17]. Tests of our simulation code were also found to predict important changes in the observed diffraction moving on and off the multilayer Bragg peaks due to interference effects, the experimental confirmations of which will also be presented here. As far as we are aware, this effect has not yet been published, and the magnitude of the effect could have important implications for those wishing to obtain quantitative information about the magnetic structures of their samples. We also begin to examine the effect of roughness and polycrystalline structure in both reflection and transmission, but due to the complexity of this topic, a full treatment will need to be left for a later paper. To fulfill the long-term aim of directly recovering the 3D magnetization distributions from a set of experimental scattering data, it will be necessary to first resolve the theme of roughness and diffuse scattering in transmission from polycrystalline grain walls, and subsequently (or in parallel) develop an iterative scheme for structure refinement.

B. Theoretical background

When working with soft x rays in multilayer samples, it is convenient to consider the sample as a stack of (imperfect) reflective surfaces, each with spatially varying reflection and transmission coefficient tensors depending upon both the local magnetism and electron density.

To find the refractive indices from the atomic scattering factors, the optical theorem [27] can be used which relates the atomic scattering factors to the total permittivity tensor ϵ as follows:

$$\epsilon = 1 + \frac{4\pi r_e}{k^2} \sum_s \rho_s \boldsymbol{F}_s, \tag{2}$$

where k is the wave number, r_e is the classical electron radius, ρ_s is the number of atoms of species n per unit volume, and $\boldsymbol{F}_s$ is the scattering tensor defined for each type of atom, and the sum is over the elemental species present. $\boldsymbol{F}_s$ can be expressed as [9–12,28]

$$\boldsymbol{F}_s = \begin{pmatrix} f^s_c & -if^s_{m1}\mathbf{M^s_z} & if^s_{m1}\mathbf{M^s_y} \\ if^s_{m1}\mathbf{M^s_z} & f^s_c & -if^s_{m1}\mathbf{M^s_x} \\ -if^s_{m1}\mathbf{M^s_y} & if^s_{m1}\mathbf{M^s_x} & f^s_c \end{pmatrix}, \tag{3}$$

where $\mathbf{M^s_i}$ are the distinct components of the magnetization for elemental species n. We may now combine Eqs. (2) and (3), introducing the magneto-optical constant for the nth element Q_s defined as

$$Q_s = \frac{-4\pi r_e \rho_s}{k^2} f^s_{m1}, \tag{4}$$

and the permittivity for the nth element as

$$\epsilon_s = 1 + \frac{4\pi r_e \rho_s}{k^2} f^s_c. \tag{5}$$

We therefore obtain the permittivity tensor for each element as

$$\epsilon_s = \epsilon_s \begin{pmatrix} 1 & iQ_s\mathbf{M^s_z} & -iQ_s\mathbf{M^s_y} \\ -iQ_s\mathbf{M^s_z} & 1 & iQ_s\mathbf{M^s_x} \\ iQ_s\mathbf{M^s_y} & -iQ_s\mathbf{M^s_x} & 1 \end{pmatrix}. \tag{6}$$

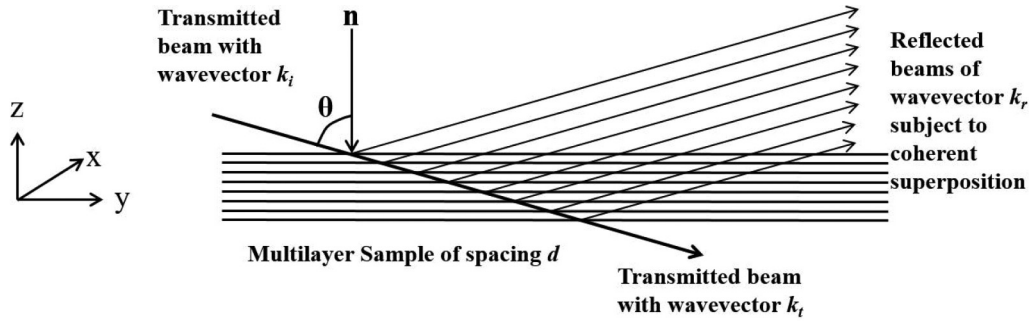

FIG. 1. y-z plane cross section of the scattering geometry of the scattering process. In the formalism of Zak *et al.* [9–12], all scattering events occur on a line parallel to the z axis; however, in the formalism to be developed in our work, the position of the scattering events is set such that all reflected rays exit the sample at the same point. The value of the sample magnetization $\boldsymbol{M}$ is allowed to freely vary throughout the 3D sample, and the angle of incidence, θ, suffers slight changes according to changes in the refractive index within the sample via Snell's law.

The refractive index for a given element for circularly polarized light can then be found from the value of Q_s to first order as [9–12]

$$n = n_0(1 \pm hgQ_s/2), \tag{7}$$

where h is the helicity of the light and takes a value -1 or 1, $n_0 = \sqrt{\epsilon_s}$ is the nondichroic refractive index for element n, and g is the cosine of the angle between the magnetization vector $\mathbf{M}$ and the Poynting vector of the incident radiation. This formalism to arrive at the magnetically dependent refractive indices is fully discussed in various references including Refs. [29,30].

With expressions for the magnetically dependent refractive indices, one is in a position to develop a formalism based upon the use of generalized Fresnel formulas, as has been done by various authors as listed in Refs. [9–12,30–34]. Being based upon the calculation of reflection and transmission coefficients at the different interfaces in a thin-film sample (for example a cobalt/palladium multilayer), this theoretical formalism has been extensively utilized in studies of the specular reflection as a function of photon energy and angle of incidence. For example, Tonnerre *et al.* [35,36] probed the thickness-dependent magnetization profile of a perpendicular exchanged system with nanometer precision in the z (out-of-plane) direction by scanning the photon energy over the absorption edges of the different elements, and also scanning the incidence angle to probe the multilayer structure. Mertins *et al.* [37] used the same matrix-based method for calculating Kerr rotation values of up to 24° on resonance in the soft x-ray regime, and also corroborated their results with experimental synchrotron data. The magnetic proximity effect was investigated in Fe/Pt bilayers with hard x rays at the Pt edge by Kuschel *et al.* [38,39], also making use of the energy and angle-dependent spectral reflectivity differences, where data analysis was performed by code developed by Macke *et al.* [29,40]. This same formalism is further generalized for a reflective slab by Zwiebler *et al.* [41] in order to probe the depth-sensitive electronic profile to atomic resolution.

A formalism was developed by Valencia *et al.* to include the interfacial roughness in the simulation [42], achieving an important improvement in fitting the observed experimental data. Elzo *et al.* [30] similarly included roughness effects in the development of their simulation scheme, with the difference that their formalism was developed using a basis of circular polarization and not linear polarization as was the case for other authors and ourselves.

C. Outline of the medium boundary matrix formalism

In this section, we outline the formalism of Zak *et al.*; however, readers wishing for a more in-depth understanding of the topic are referred to primary sources of Refs. [9–12,30,32–34]. The general geometry of the scattering process is shown in Fig. 1. At the interface, the tangential components of the electric and magnetic fields E_x, E_y, H_x, and H_y are conserved, and may be expressed together as a set in the matrix

$$\boldsymbol{L} = \begin{pmatrix} E_x \\ E_y \\ H_x \\ H_y \end{pmatrix}. \tag{8}$$

At the same time, the components of the incoming and outgoing waves may be expressed in terms of their circular helicities or perpendicular (σ) and parallel (π) components with respect to the scattering plane which in the geometry chosen here is the y-z plane. Most authors have expressed the medium boundary matrix on a basis of linear polarization as we will here; however, Elzo *et al.* [30] used a circular polarization basis. With linear polarization, the electric fields of the incoming and outgoing (reflected) wave are expressed via the P_{in} matrix as

$$\boldsymbol{P}_{\text{in}} = \begin{pmatrix} E_\sigma^i \\ E_\pi^i \\ E_\sigma^r \\ E_\pi^r \end{pmatrix}. \tag{9}$$

These two matrices are connected by the medium boundary matrix A according to

$$\boldsymbol{L} = A\boldsymbol{P}_{\text{in}}. \tag{10}$$

Using the notation of Qiu and Bader [34], where $\mathbf{Q_s} = [Q_s^x, Q_s^y, Q_s^z] = Q_s\mathbf{M}$ and n_0 is the nondichroic refractive

index, we have the medium boundary matrix defined as

$$A_i = \begin{pmatrix} 1 & 0 & 1 & 0 \\ \frac{i}{2}\left[-Q_s^y \tan\theta(1+\cos^2\theta) + Q_s^z \sin^2\theta\right] & \cos\theta + iQ_s^x \sin\theta & \frac{i}{2}\left[Q_s^y \tan\theta(1+\cos^2\theta) + Q_s^z \sin^2\theta\right] & -\cos\theta + iQ_s^x \sin\theta \\ \frac{in_0}{2}\left(Q_s^y \sin\theta + Q_s^z \cos\theta\right) & -n_0 & \frac{in_0}{2}\left(Q_s^y \sin\theta - Q_s^z \cos\theta\right) & -n_0 \\ n_0 \cos\theta & \frac{in_0}{2}\left(Q_s^y \tan\theta + Q_s^z\right) & -n_0 \cos\theta & \frac{-in_0}{2}\left(Q_s^y \tan\theta - Q_s^z\right) \end{pmatrix}. \tag{11}$$

With the medium boundary matrix, we are thus in the position to express the radiation amplitudes on both sides of a reflecting matrix as follows: We first apply Eq. (10) for the interface between material 1 and material 2, which either can be magnetic with values $Q_s \neq 0$, or can be nonmagnetic where $Q_s = 0$:

$$A_1 \boldsymbol{P}_1 = A_2 \boldsymbol{P}_2. \tag{12}$$

From here, we may express $\mathbf{P_1}$ in terms of $\mathbf{P_2}$ as

$$\boldsymbol{P}_1 = A_1^{-1} A_2 \boldsymbol{P}_2 = M \boldsymbol{P}_2. \tag{13}$$

The matrix M is a 4×4 matrix which may be expressed in terms of four 2×2 matrices

$$M = \begin{pmatrix} G & H \\ I & J \end{pmatrix}, \tag{14}$$

where I is not to be confused with the identity matrix, and from which the transmission and reflection coefficients can be calculated according to

$$T = G^{-1} = \begin{pmatrix} t_{\sigma\sigma} & t_{\sigma\pi} \\ t_{\pi\sigma} & t_{\pi\pi} \end{pmatrix}, \tag{15}$$

and

$$R = IG^{-1} = \begin{pmatrix} r_{\sigma\sigma} & r_{\sigma\pi} \\ r_{\pi\sigma} & r_{\pi\pi} \end{pmatrix}. \tag{16}$$

With the reflection and transmission coefficients on hand for a single interface, it is immediately apparent how one may calculate the resonant scattering from a single ideal interface between two materials, or between a vacuum and the surface of a single-layer magnetic film. We compute the spatial distribution of the magnetization vector **M**, over the surface of the film, and then calculate the boundary matrices for both materials at each simulation pixel. Diffraction may then be calculated from the reflection coefficients given the polarization of the incident light, and the spatial array of reflection coefficients calculated at each point using the above-described procedure (for example, from a perpendicular anisotropy stripe domain sample with closure domains where the diffraction will produce the typical asymmetric first-order peaks, for example, in Ref. [2]). In cases where the sample at hand is a smooth and optically thick single-layer sample (not a multilayer), no more work is necessary to simulate the scattering from the surface layer. Such was the state of the algorithm used for the modeling of scattering in the work of Pianciola *et al.* [23]. For multilayer samples, the treatment is more complex and is presented in the subsequent section.

D. Multilayer sample treatment

Due to the fact that the pair of medium boundary matrices expresses the electromagnetic field on one side of an interface in terms of the field on the other side of this interface, one may extend the formalism to a multilayer system of N such layers grown on a substrate by creating a stack of such interfaces, and making use of the medium propagation matrix to move from one interface to another [9–12,30,32–34]:

$$\boldsymbol{A}_i \boldsymbol{P}_i = \boldsymbol{A}_1 \boldsymbol{D}_1 \boldsymbol{A}_1^{-1} \boldsymbol{A}_2 \boldsymbol{D}_2 \boldsymbol{A}_2^{-1} \cdots \boldsymbol{A}_N^{-1} \boldsymbol{A}_s \boldsymbol{P}_s. \tag{17}$$

This expression makes use of the medium propagation matrix to define the electromagnetic field at one interface in terms of the field at a neighboring interface after having propagated through any one of the layers of thickness d. The medium propagation matrix is expressed here in terms of a linear polarization basis using the notation of Qiu and Bader [34]; however, in the work of Elzo *et al.* [30], a circular polarization basis is used in which this matrix appears diagonal. It is for this reason that the circular basis is used almost exclusively when working in transmission geometry due to the absence of crosstalk between polarization states. The medium propagation matrix for the ith layer D_i is defined as

$$D_i = \begin{pmatrix} U\cos\delta_i & U\sin\delta_i & 0 & 0 \\ -U\sin\delta_i & U\cos\delta_i & 0 & 0 \\ 0 & 0 & U^{-1}\cos\delta_r & -U^{-1}\sin\delta_r \\ 0 & 0 & U^{-1}\sin\delta_r & -U^{-1}\cos\delta_r \end{pmatrix}, \tag{18}$$

where

$$U = \exp(-ikd\cos\theta), \tag{19}$$

with θ representing the angle of incidence *within each layer*, and

$$\delta_i = \frac{kd}{2}\left(Q_s^y \tan\theta + Q_z\right), \quad \delta_r = \frac{kd}{2}\left(Q_s^y \tan\theta - Q_s^z\right). \tag{20}$$

Studying the form of the medium propagation matrix in conjunction with the scattering geometry, one notes that the propagation distance within the material appears as $d\cos\theta$, which tends towards zero at grazing incidence. This is because the formalism of Refs. [9–12,30,32–34] considers the reflection events occurring in a column parallel to the z direction, and does not consider the absorption within the material prior to and immediately following a reflection event—absorption which occurs over a length of $z_i/\cos\theta$, where z_i is the depth of the ith layer. In the case of incoherent multiple scattering from thick samples, a formalism was developed and experimentally tested by Dorazio *et al.* [43,44], where the reflections from each interface are summed after their amplitudes and Faraday rotations are adjusted to account for the transmission within the sample before and after reflection. In the

soft x-ray regime which is the main focus for this work, it appears as if a similar approach was used by Li *et al.* [19] for analyzing the depth-dependent domain wall profile in the skyrmion hosting multilayer system $[\mathrm{Ta}|\mathrm{CoFeB}|\mathrm{MgO}]_N$. This work, however, lacks a formal analysis section and mentions only the exponential attenuation of the reflection from multilayers deeper within the sample. Their work does, however, mention the increased penetration achieved from working at an incidence angle further from grazing incidence, thus allowing depth-dependent information to be extracted by varying the incidence angle. Scanning the photon energy over the absorption edge can also be used for a similar effect, as will be demonstrated below in the experimental section. This simple attenuation correction can be considered a manner of applying the DWBA [45] to first order, and our approach will go one step further by considering spatial variations in the sample magnetization when calculating the attenuation and phase shift of the x rays passing through the sample.

II. SIMULATIONS: PROCEDURE AND CONSIDERATIONS

A. The recipe to calculate the diffraction pattern in reflection conditions

In this section, we present our numerical recipe for the calculation of diffraction patterns in reflection geometry.

Step 1. Download the atomic scattering factor files for all elements in your sample. These data may be found for all elements at the Center for X-ray Optics (CXRO) website [46]; however, readers must be aware that this database does not include the effects of resonance occurring when the x-ray energy matches a core level absorption. Near such absorption edges, one must use one's own or previously published x-ray absorption data to complement the values downloaded from the CXRO website. Simulations in this paper were performed with atomic scattering factor values measured from x-ray magnetic circular dichroism (XMCD) measurements on cobalt films at the SEXTANTS beam line at SOLEIL. Readers should beware of differing energy calibrations between different facilities, and use the measured position of the absorption edge and not a fixed energy as the reference point.

Step 2. From experimental x-ray absorption data, one can directly deduce the imaginary parts of the refractive indices, but to find the corresponding real parts, the Kramers-Kronig relations must be used. Their application requires the splicing of experimental XMCD data with the off-resonance refractive index and/or atomic scattering factor data. We performed this step assuming that, at the edge of the resonant region, the refractive indices retrieved from the two sources must be equal.

Step 3. To initialize the simulation procedure, one must have on hand a model magnetization distribution. This should be defined over the planes of each interface in the multilayer sample due to the physical significance of each interface. It is ideal in this step to use micromagnetic simulations in order to provide a physical basis to the model chosen, with a method for extrapolating a localized micromagnetic simulation over the up to several hundred micrometer size of a typical x-ray scattering experiment published previously in Refs. [6,25,47]. It is alternatively possible to define the magnetization distribution in geometric terms of average domain width, domain-wall width, and domain-wall magnetization angle varying between zero for Bloch and $\pi/2$ for Néel. In order to proceed, one requires at this step a 3D vector field of the magnetization vector $\boldsymbol{M}$ evaluated at each 3D pixel in the sample under study, with the example used for simulating the subsequent experimental work shown in Fig. 2.

Step 4. From the 3D magnetization vector field, applying Eqs. (11)–(16) at each and every point on the x-y plane of each interface, one obtains a stack of two-dimensional maps of the reflection coefficients, as is illustrated for a surface layer with Néel-type domain walls in Fig. 3. Users must be careful in this case to recalculate using the appropriate angle of incidence, θ_{el}, within each elemental layer (el) using Snell's law for an angle of incidence in free space, θ_i. To deal with the complex refractive indices, a generalized form of Snell's law was used in this work, found in Eq. (15) of Ref. [48],

$$\sin(\theta'_{el}) = \frac{\sqrt{2}\sin\theta_i}{\sqrt{n^2-k^2+\sin^2(\theta_i)+\sqrt{(n^2-k^2-\sin^2\theta_i)^2+4n^2k^2}}}, \tag{21}$$

where θ_i is the free-space angle of incidence, θ'_{el} is the angle within the layer of index of refraction n, and k is the wavenumber.

An example of these reflection coefficients is shown in Fig. 3 for the first layer where the domain-wall type is Néel, but where a longitudinal component of the magnetization is present at the points where the stripes bend.

Step 5. Prior to and after suffering a reflection event, the x rays which reflect from buried interfaces undergo attenuation and Faraday rotation due to transmission through a magnetized medium, with this transmission incorporated using the following algebra.

First we extract the quadrants of the medium transmission matrix D defined in Eq. (18) relating to the forward propagation of incident i and reflected r waves:

$$D^i_{el} = \begin{pmatrix} U\cos\delta_i & U\sin\delta_i \\ -U\sin\delta_i & U\cos\delta_i \end{pmatrix}, \tag{22}$$

$$D^r_{el} = \begin{pmatrix} U\cos\delta_r & U\sin\delta_r \\ -U\sin\delta_r & U\cos\delta_r \end{pmatrix}. \tag{23}$$

We modify U, δ_i, and δ_r compared with their original definitions in Eqs. (18)–(20) in order to account for the true path length through an imperfect layer of thickness $d+\delta d(x,y,z)$, where $\delta d(x,y,z)$ is the thickness deviation from a perfectly smooth layer:

$$U = \exp\left(\frac{-ik(d+\delta d(x,y,z))}{\cos\theta_{el}}\right) \tag{24}$$

and

$$\delta_i = \frac{k(d+\delta d(x,y,z))}{2}\left(Q^y_s\tan\theta_{el}+Q^z_s\right), \tag{25}$$

$$\delta_r = \frac{k(d+\delta d(x,y,z))}{2}\left(Q^y_s\tan\theta_{el}-Q^z_s\right). \tag{26}$$

For computational simplicity, we assumed in calculations that the magnetization along the optical paths of the incoming

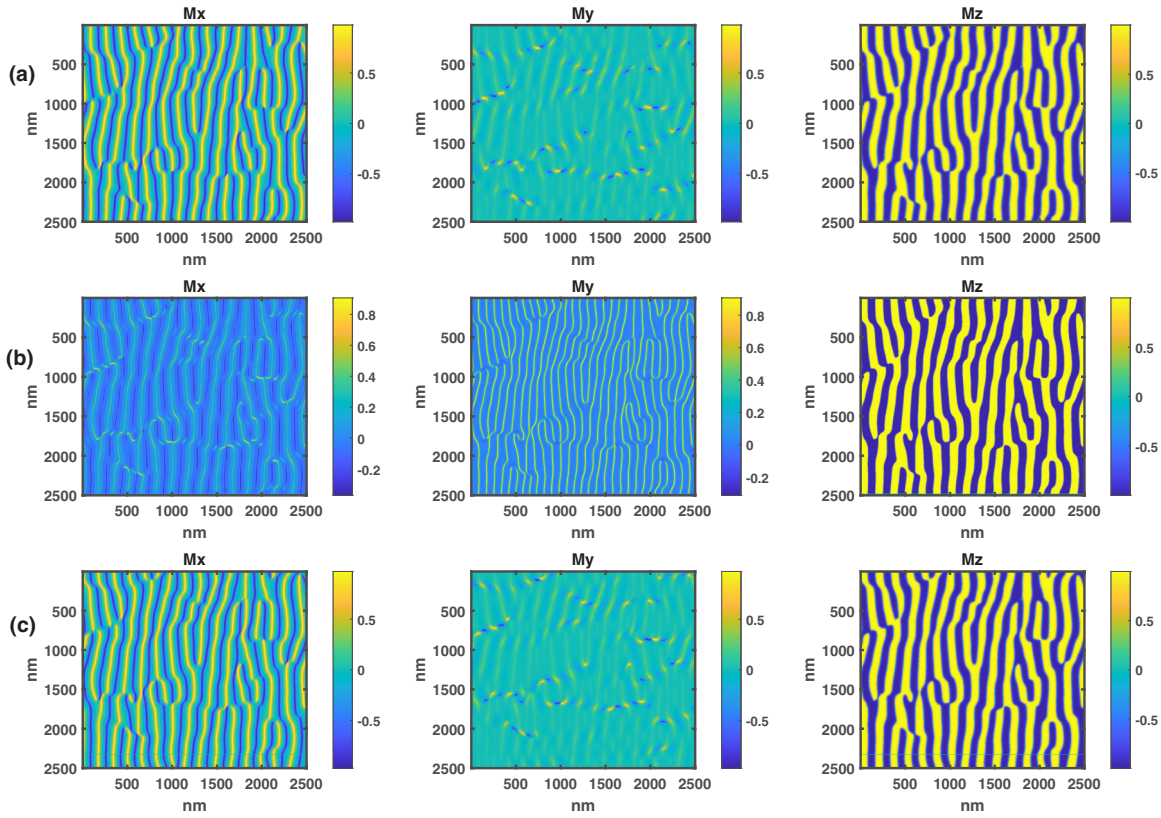

FIG. 2. Simulated distribution of the magnetization (a) on the top layer of the sample, (b) through the middle of the sample, and (c) on the sample/substrate interface. Note the reversal of sign in M_x between the top and bottom layers of the sample, and the fact that M_y is dominant in the middle of the sample. This demonstrates the hybrid nature of the domain-wall structure with Néel type (M_z, M_x, M_z) on the surfaces, and Bloch type (M_z, M_y, M_z) in the middle.

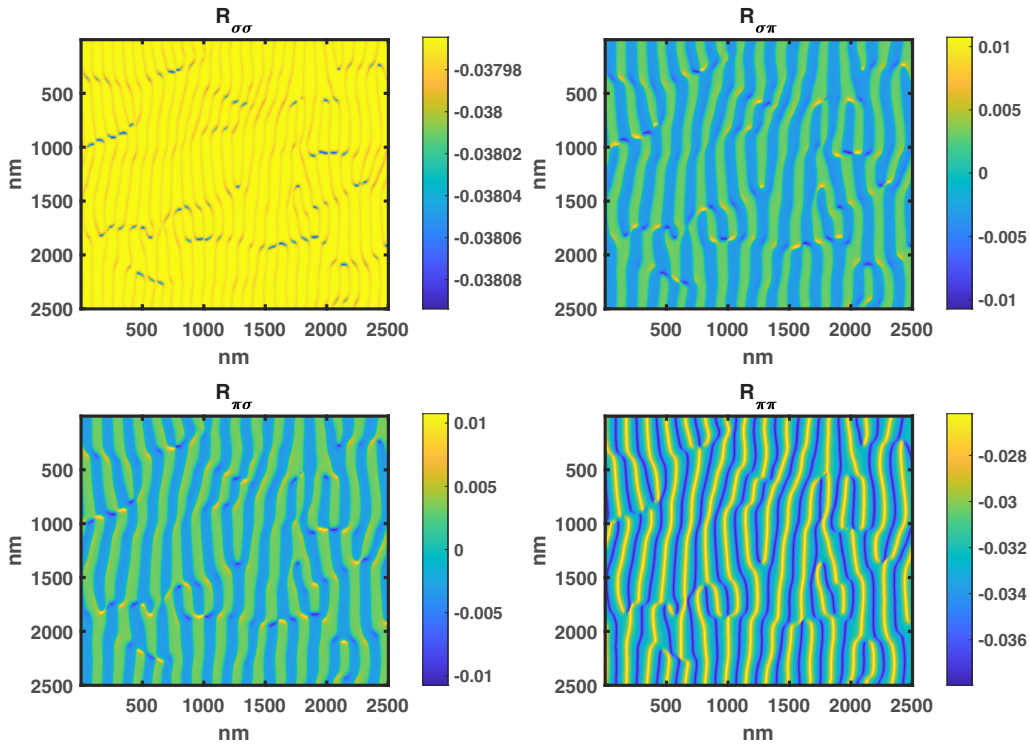

FIG. 3. Real parts of the reflection coefficients for the magnetic interface closest to the surface. The incidence angle was equivalent to the nominal first multilayer Bragg angle for this thin film; 16.5° from grazing incidence.

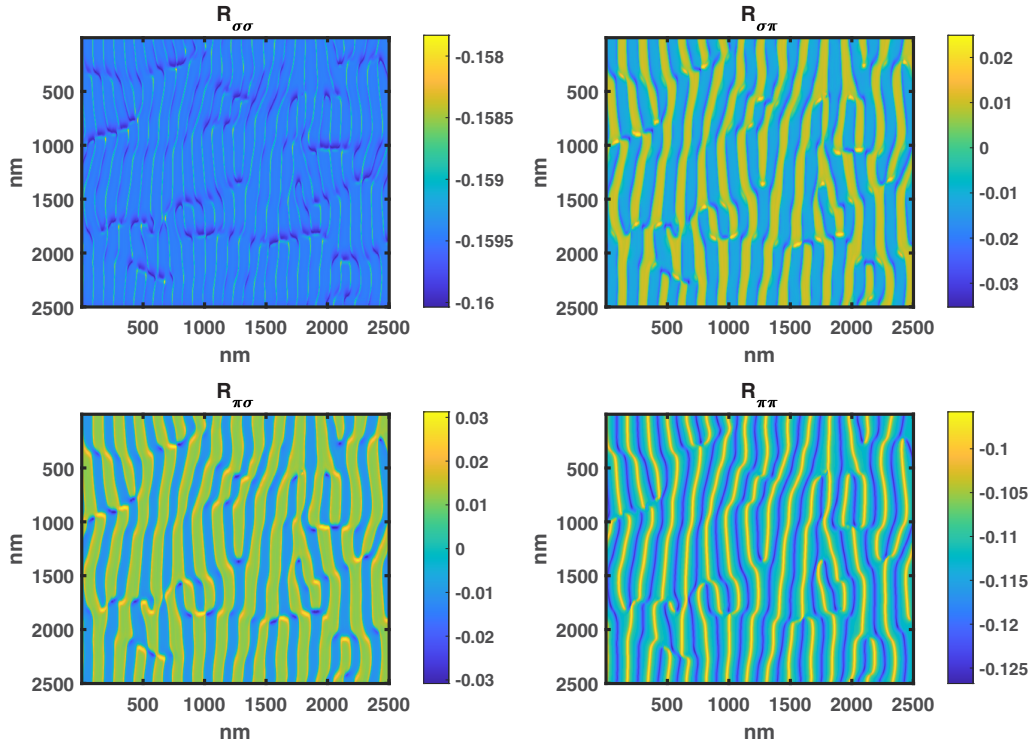

FIG. 4. Real parts of the total effective reflection coefficients of the entire thin film. The array of effective reflection coefficients shown here is the sum of phase-matched reflection coefficients for each of the magnetic interfaces in the sample. The incidence angle was equivalent to the first nominal Bragg angle for this thin film, 16.5° from grazing incidence.

and outgoing waves is identical, as is approximately the case for the stripe domain samples studied here. The outgoing wave reflected from the interface between layer N and layer $N+1$ buried within the sample, where the incident wave is given by

$$\boldsymbol{P}_{\text{in}} = \begin{pmatrix} E_\sigma^i \\ E_\pi^i \end{pmatrix}, \tag{27}$$

will therefore arrive at the surface after having been subject to the following series of matrix operators for each layer in the multilayer sample. For the nonmagnetic layers, due to the fact that the D matrices are diagonal, the matrix multiplication may be replaced with scalar multiplication:

$$\boldsymbol{P}_{\text{out}} = \prod D_1^r D_2^r \cdots D_n^r R D_n^i \cdots D_2^i D_1^i \boldsymbol{P}_{\text{in}}. \tag{28}$$

In order to accurately reproduce the multilayer interference phenomena, it is necessary to calculate the phase of the incident radiation at the point of insertion relative to the phase on exit from the multilayer by calculating the optical path difference ΔR. For a multilayer sample of different refractive indices in each layer, this may be performed in a recursive manner for each successive layer of thickness d_{el}:

$$\Delta R_{n+1} = 2(d_{el} + \delta d_r(x, y, z)) \tan\theta_{el} \sin\theta_i + \Delta R_n. \tag{29}$$

The phase shift on entry relative to the phase at exit may then be calculated as

$$\Delta\phi = e^{\frac{2\pi\Delta R}{\lambda}}. \tag{30}$$

Readers are reminded that the phase shift of the beam as it passes through the magnetized sample is also accounted for by Eq. (28).

Step 6. After summing the phase-shifted and attenuated wave fields from each interface within the sample at the level of the surface, the resulting total wave field may be propagated to the detector using standard free-space propagation. The effective combined reflection coefficients representing the phase-matched sum of all reflections are shown in Fig. 4, and may be used to calculate the outgoing wave field given an incoming wave field. One should be aware that the application of a simple Fourier transform for the free-space propagation gives an acceptable performance in situations where magnetic domains are aligned parallel to the scattering plane; however, it does not reproduce exactly the experimentally observed diffraction from features perpendicular to the scattering plane. This is due to Ewald sphere curvature, and causes the effective angle of incidence to depend upon the value of q_y in the resulting diffraction pattern. Variations of the effective angle of incidence with q_y increase as the angle of incidence approaches grazing incidence.

For a 20-layer sample and a 1024×1024 array, the computation time with MATLAB on a Hewlett Packard workstation with 12 cores from the year 2014 was approximately 7 min. In the case where it is sufficient to simulate with perfectly aligned stripe domains of identical size, speed can be increased by using a much smaller array size.

B. Introduction to the theme of roughness in simulations

The above-described algorithm when $\delta d(x, y, z) = 0$ deals with the ideal situation where the sample can be described as a regular stack of perfectly smooth atomic layers. In practice, however, such stacks do not exist, and one must take into

account the influence of roughness and irregular spacing of the atomic layers. A dimpled surface in the x-y plane will produce a diffuse scattering background or coherent speckle depending upon the coherence of the incident radiation. This diffuse scattering will appear underneath and possibly interfere with any magnetic peaks detected in the scattering pattern; especially at low spatial frequencies, it will also weaken the interference effects between the different layers in the sample. A full treatment of surface roughness can be found in Refs. [30,42,49,50], where the treatment was statistically based upon a Gaussian distribution of the spatial deviations from a perfectly flat multilayer stack. In our work, because we explicitly generate a multilayer stack with a given magnetic domain pattern, this roughness is accounted for directly by adjusting the z spacing between each layer on a pixel-by-pixel basis according to a random roughness function $\delta d(x, y, z)$ of amplitude and planar spatial frequency distribution which best reproduce the observed experimental background.

During the transmission through the sample before and after a reflection event, it is also likely that there are further losses not accounted for by the imaginary part of the refractive index due to diffuse scattering from grain boundaries, strain, and other crystal imperfections. Such diffuse scattering was observed in previous work [6,25], and is of increasing importance as the incidence angle approaches 90° (as measured from the normal). The magnitude of this effect is expected to depend on the photon energy, the angle of incidence, and the specific sample fabrication characteristics; we are of the opinion that a full investigation of this factor is warranted. We note that the custom thus far of subtracting the experimental diffuse background by cubic spline fitting or similar methods also includes the implicit assumption that the diffuse background and magnetic scattering signal add incoherently. Such an assumption, however, is not valid, as is demonstrated by the fact that Fourier transform holography [51,52] of magnetic samples in transmission geometry is an established field, and depends upon the interference between the magnetic signal and the nonmagnetic reference signal. The effects are, however, small in cases where the magnetic scattering signal is much stronger than the diffuse background, and where the spatial coherence length is much less than the spot size—conditions which are met for most RXMS experiments.

C. Transmission geometry

In most experimental cases of interest where scattering is to be used, reflection geometry is a more sensitive probe due to the strong differential contrast between the different polarization states. Transmission geometry scattering, which was studied elsewhere in more detail [6,25], is, however, of interest particularly where one is working with single-layer samples where reflection would only occur from the top surface (and in some cases from the substrate), or where an imaging-type experiment is proposed such as that of Donnelly *et al.* [53]. In transmission geometry it is necessary to rotate the sample in order to extract 3D information about the sample, whereas in the case of reflection geometry, one may tune the x-ray energy on and off resonance to enable differing amounts of depth sensitivity. For this configuration, the simulated sample should be defined on a cubic matrix, which must then be interpolated in a series of diagonal slices perpendicular to the vector of propagation of the incident beam and subject to multiple slice propagation [54]. Working in a circular polarization basis, the refractive index is given by utilizing Eq. (7), allowing the complex transmission function for the projection over a given slice of thickness δx to be expressed as

$$T = \exp\left(\frac{-2\pi}{\lambda} i(n_0(1 \pm hgQ_s/2) - 1)\delta x\right). \tag{31}$$

This process accurately reproduces the deviations from simple projection approximation modeling observed in experiments due to curvature of the Ewald sphere, and enhanced absorption of diffracted x rays in the direction towards the sample due to an increased optical path length within the sample. Once clear of the sample, Fourier-transform-based free-space propagation may be used to propagate to the detector plane, with no caveats as in the case of reflection geometry, due to the wave field being defined over a plane parallel to the direction of beam propagation. It was our original intention to use this multiple-slice propagation as the approach for the reflection geometry work presented here, adding reflection events at each interface as the beam passed through the sample. This was, however, found to be both numerically unstable due to observed "diffraction" from the pixel matrix, and extremely slow due to the large number of Fourier transforms which needed to be evaluated. As a result, this multislice propagation approach was discarded for our approach based on projection approximation transmission and a single reflection event per reflected beam.

D. Treatment of x-ray coherence

Levels of spatial coherence of synchrotron sources have been steadily increasing, with the newest diffraction-limited sources expected to provide close to full coherence over the size of the beam. In the case of full coherence, the task of simulating the diffraction is straightforward: The Huygens-Fresnel principle permits one to calculate diffraction via free-space propagation of the outgoing wave field (in both reflection and transmission geometry). In the case of partially coherent illumination, the most straightforward manner in which to simulate the resulting diffraction is via the coherent mode expansion [55], which in the case of a disordered and statistically stationary sample may be approximated by summing the results of a set of realizations of the code assuming a coherent beam over the region of each simulation—each simulation performed with a different real-space domain configuration. This latter approach was used in an approximate manner by Flewett *et al.* [25], simulating partial coherence by summing a series of ten realizations of the simulation with coherent radiation, but using a different matrix of random numbers with which to simulate the magnetic domain pattern. This same approach will be used here for the simulations where a disordered magnetic domain pattern is used, and in the case where roughness is present.

III. EXPERIMENTAL VALIDATION

The approach described in the previous section was developed to respond to need to analyze the x-ray reflective

scattering data from a single layer by Pianciola *et al.* [23], and more recently for a multilayer system incorporating the DWBA [22,24]. The work of Burgos-Parra *et al.* [22] deals with a stripe domain system with an external field applied along the length of the stripes, and the work of Léveille *et al.* [24] an antiferromagnetic worm domain system where the magnetic signal is strongest at 1/2 and 3/2 of the multilayer Bragg angle. In contrast with the above-cited examples where the general aim of their work was to use RXMS to study the magnetic properties of the sample, the experimental tests presented here were designed with the explicit aim of probing the robustness of our theoretical framework.

A. Experimental and simulation conditions

Our tests were performed using the same $Ta_1|Pt_{0.8}[Co_{0.8}|(Al_2O_3)_1|\ Pt_1]_{20rep}|Pt_2$ multilayer as in the work of Burgos-Parra *et al.* (where the numbers in subscript are thicknesses in nanometers except for the 20, which is the number of repetitions) [22]. The RXMS measurements were performed at the RESOXS diffractometer [56] at the SEXTANTS beam line [57] of the synchrotron SOLEIL in France. They were conducted in reflection geometry with both circular polarizations at energies between 775 and 781 eV, with the diffracted x rays collected using a Peltier-cooled square CCD detector covering 6.1° at the working distance of this study. For all measurements the exit slits were set at 25 μm with a resolving power around 5000, and total exposure times were 5 s at the first Bragg angle, 15 s for the second Bragg angle, and 100 s for the third Bragg angle. For seeding our simulation RXMS code, micromagnetic simulations were performed using the energy minimization procedure implemented in MUMAX3 to generate a domain-wall profile [14]. The parameters used were $A = 9.5$ pJ m^{-1} for the Heisenberg exchange, $D = 1$ mJ m^{-2} for the DMI constant, $Ku = 1.43$ MJ m^{-3} for the uniaxial anisotropy along the z axis and $Ms = 1.37$ MA m^{-1} for the saturation magnetization of the cobalt layers. A cross section of a single domain wall obtained with the simulation is shown in Fig. 5(a), where the skew structure in the out-of-plane direction typical of a nonzero DMI [17] can be appreciated. In Fig. 5(b), we show the specular reflection at 778 eV as a function of incidence angle, from which we determined the three Bragg angles at which subsequent measurements were made. It should be noted that for experimental measurements, the Bragg angles found via specular reflection were used, whereas for simulations we used the Bragg angles calculated from the nominal sample thickness. The small difference between the two (of 1° for the first Bragg angle) is due to a slight calibration imperfection in the sputtering system. In Figs. 5(c) and 5(d) we show values of δ and β, the deviations from unity of the refractive index n as a function of incidence energy according to $n = 1 - \delta - i\beta$. In Fig. 5(c) we show the values of the nonmagnetic part caused by fluctuations in f_c^s and in Fig. 5(d) the values corresponding to the magnetic part caused by fluctuations in f_{m1}^s. In Fig. 5(e), we show panels of the raw scattering pattern at 778 eV for each Bragg angle (without correcting for the projection angle in the q_y direction). For subsequent analysis, the scattered intensity was integrated over the q_y direction, which was made possible due to the fact that we are working with a stripe domain sample. Had a worm domain or highly disordered stripe pattern been used as in Ref. [24], such integration would result in a loss of information.

Our first test was the examination of the variation of the scattering pattern moving off the multilayer Bragg angle in order to evaluate the importance of interference effects beyond the well-known reduction of signal strength due to the loss of constructive interference. This not only served the role of uncovering new physics, but also for verifying the correctness of step 5 of our algorithm—the part related to the phase matching between the beams reflected from different layers. The second test involved energy scans over a 6-eV range across the resonance at the first three multilayer Bragg angles to evaluate the suitability of our algorithm for extracting depth-sensitive information about the magnetization distribution, and to evaluate the influence of interface roughness and polycrystalline structure on the experimental outcome.

B. Interference effects moving off the multilayer Bragg angle

It is known that working at the multilayer Bragg angle is advisable in order to increase the signal-to-noise ratio; however, when moving off the Bragg angle not only is the diffracted intensity reduced, but major qualitative changes in the scattering signal are observed. In the first test with results in Fig. 6, we looked both at the first multilayer Bragg angle, and 1° off the Bragg angle towards grazing incidence, both at zero field, and with an external field of 1900 G in plane along the $\vec{y}$ direction applied.

In Fig. 6, in addition to the expected signal reduction observed moving off the Bragg angle, there are three features which readers should take note of:

(1) The degree of asymmetry present in the first-order peaks both with and without external field defined as $(I_l - I_r)/(I_l + I_r)$ increases by approximately 20 percentage points as one moves *off* the Bragg angle.

(2) The dichroism observed in the second-order peaks where field is applied is much stronger on the Bragg angle compared with being off the Bragg angle.

(3) The experimental diffuse background in the case with field applied is approximately double in one polarity compared with the other. This dichroism has been observed in specular reflection [35,36], and one may consider the background to be due to roughness and scattering in transmission from the polycrystalline grain walls causing broadening of the specular peak.

The theoretical results were simulated assuming a root-mean-square (RMS) interfacial roughness of 0.7 Å with a Lorentzian profile, and with the imaginary part of the refractive index β increased by $\Delta\beta = 0.001$ to approximate losses due to diffuse scattering in transmission. Each theoretical plot was generated as the ensemble average of ten simulations for different randomly generated magnetic domain patterns similar to those shown in Fig. 2. Here in Fig. 6, the observations regarding the changes in the first- and second-order peaks can be explained by interference between the different waves emitted from each interface in the multilayer sample. The increase in observed asymmetry of the first-order peak arises from the change of sign in the asymmetry of the reflected waves from the Néel part of the domain wall close to the substrate in the sample where the chirality is opposite

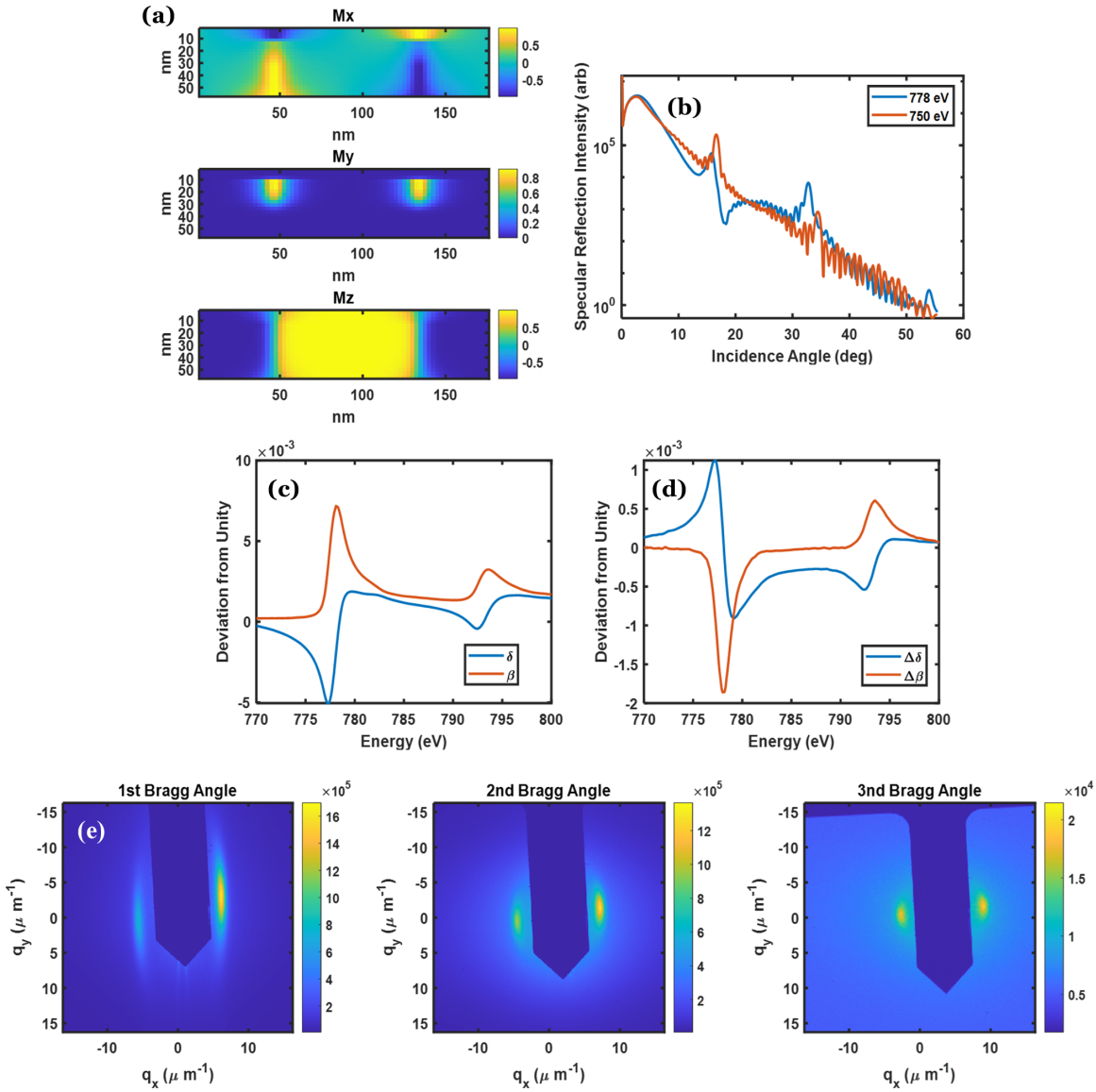

FIG. 5. (a) Cross sections in the x-z plane through one ideal magnetic unit cell used for generating the simulations. Note the Bloch wall being situated in the upper part of the film. (b) Specular reflection curves both on resonance (778 eV) and off resonance (750 eV). (c) δ and β values for cobalt used in the simulations (measured at the SEXTANTS beam line of SOLEIL). (d) The magnetic deviations of the refractive index as a function of energy where the Poynting vector is parallel to the magnetization vector. (e) Raw RXMS measurements for the first, second, and third Bragg angles at the incidence angles determined by the specular reflection scan (15.5°, 33°, and 53.8°).

compared to the Néel part of the domain wall close to the surface [17,19]. Conceptually, for a given helicity and when the sample is aligned at the Bragg angle, at the detector we have constructive superposition between the positive asymmetry $(I_l - I_r)/(I_l + I_r)$ contributions from the top layers of the sample, the zero asymmetry from the middle layers with a Bloch domain wall, and negative asymmetry from the contributions near to the substrate. The sum of these gives us the measured scattering patterns with moderate asymmetry as seen in Figs. 6(a) and 6(b). When we move off the Bragg angle, however, there is a phase shift between the contributions from each layer, and when the contributions from the lower layers of the sample with the opposite asymmetry to the top layers are superimposed out of phase, the result is not a reduction in the asymmetry but rather a reduction in the intensity and an *increase* in the asymmetry. This is an important result not only because it demonstrates the key role that multilayer interference plays in the observed scattering patterns, but also because it demonstrates the potential future utility of exploiting such interference for a more precise characterization of the samples in the z direction.

C. Born approximation versus distorted-wave Born approximation: Explanation of dichroism observed with applied longitudinal field in second-order scattering peaks

In the previous section, a notable dichroism was observed in the second-order scattering peaks when observed at the Bragg angle—a phenomenon which was extensively studied by Burgos-Parra *et al.* in their work developed in parallel with this paper [22]. In theoretical terms, this dichroism at second (and fourth) order was not explained solely by the spatial differences in the reflection coefficients across each plane in

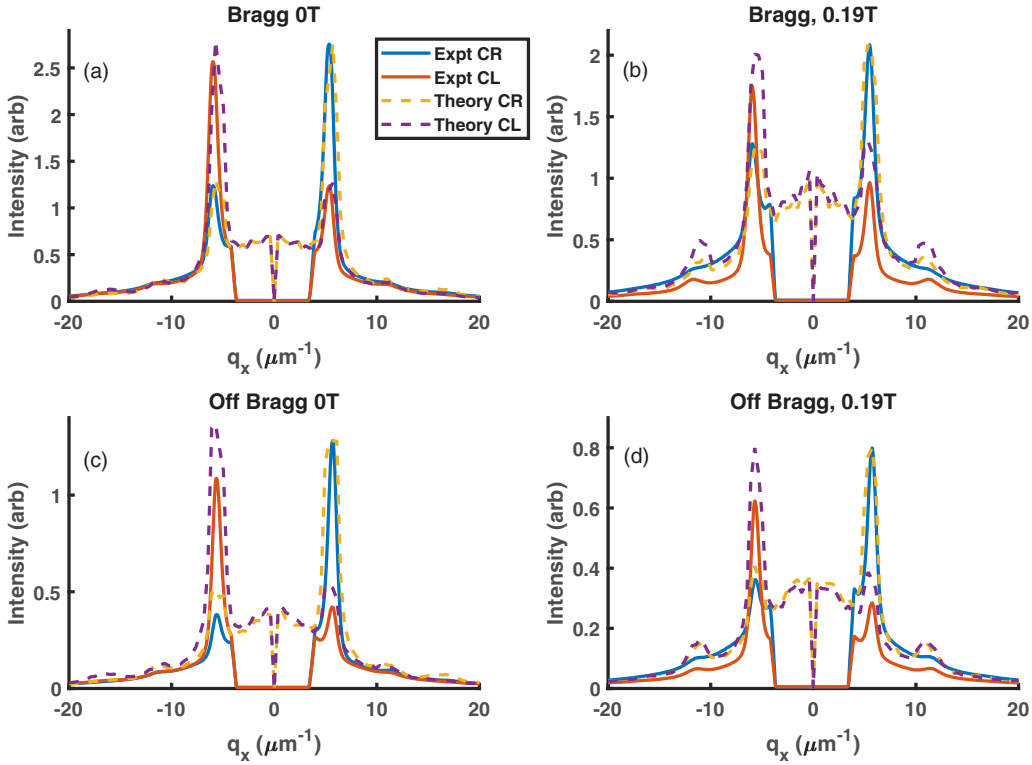

FIG. 6. Experimental scattering data (integrated over the q_y direction) with and without an in-plane applied field on and off the multilayer Bragg angle. The four lines on each graph represent left and right polarized light for both experiment (solid) and theory (dashed) lines. The results (a) at zero field on the Bragg angle, (b) at a field of 0.19 T on the Bragg angle, (c) at zero field but 1° off the Bragg angle, and (d) at 0.19 T and 1° off the Bragg angle.

the multilayer, but rather only by including the differential absorption in transmission according to the incident polarization and magnetization vector. In fact, it was the need to explain this second-order dichroism in the work of Burgos-Parra *et al.* [22] which brought about the addition of the DWBA to the simulation recipe discussed here—an addition which approximately doubled the computation time. This is demonstrated in Fig. 7, where theoretical curves are shown for both the BA case and the DWBA case. Only in the DWBA case was it found possible to reproduce the dichroism observed experimentally between the two polarization states at second order. The nature of the dichroism at second and fourth order is distinct from that at first and third order: At odd orders, we observe the characteristic left-right asymmetry which flips with a change of polarization; however, at even orders we observe left-right symmetric diffraction peaks whose intensity depends upon the polarization. From a semantic point of view, it is perhaps not appropriate to be talking about a

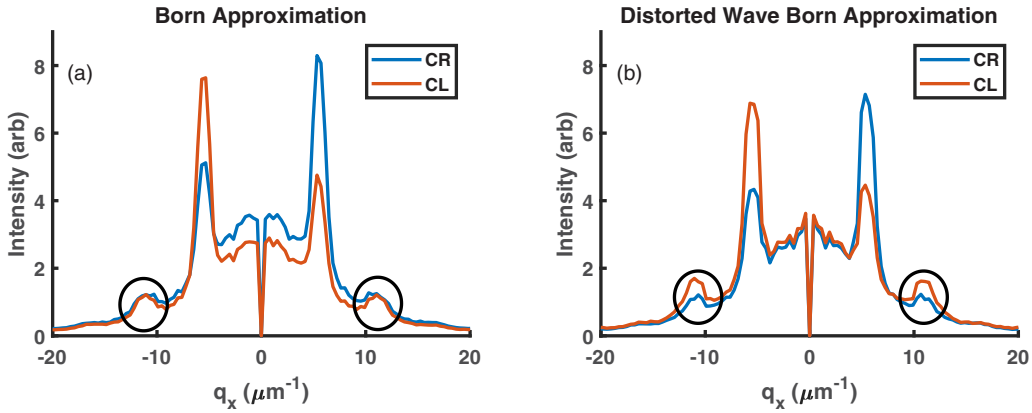

FIG. 7. Simulated scattering scans with a 0.19-T external field applied along the magnetic stripe axis (a) using the BA accounting for the reduced contribution from buried interfaces due to x-ray absorption, and (b) using the DWBA as presented in the text. The plots show the simulated scattering summed over the q_y direction, with the second-order peaks highlighted to show the difference between using the BA and using the DWBA.

pure reflection configuration in this case, but rather a situation where reflection and transmission are combined—the strong second-order peaks observed due to the Bloch walls being evidence of the transmission component at play. It will be interesting in the near future to combine reflection with transmission measurements in order to obtain a more precise quantification of the size of the Bloch walls, and also obtain a better quantification of the role of the polycrystalline nature of the sample in the generation of the background signal. The explanation of this dichroism in the second-order peaks, and the finding that it arises due to differential transmission along the Bloch walls and not merely due to differences in the reflection coefficients, is one of the chief results of this work.

D. Studying depth penetration with energy scans at different Bragg angles

This work, inspired by that of Refs. [19,26], looks to evaluate the extraction of information in the $\vec{z}$ direction, hopefully extending from the qualitative treatment of Refs. [19,26] to a more quantitative treatment. A further inspiration was based on the work of Legrand *et al.* [17], where the z position of the Bloch wall was found to be directly related to the value of the DMI. Should one be able to quantitatively determine the value of the Bloch wall, then it could be possible to determine the DMI by means of resonant x-ray scattering, complementing the existing techniques, notable Brillouin light scattering [58,59] or domain wall creep [60]. As will be seen in the following results and accompanying discussions, the full quantification of the real effective penetration depth will be necessary before a quantitative measurement of the DMI can be made.

For this part of the investigation, we measured the resonant scattering data at the first three multilayer Bragg angles of our hybrid Néel/Bloch/Néel domain-wall sample, with the incidence angles determined by the specular reflection scan shown in Fig. 5(b). The energy was scanned from 775 to 781 eV in 0.2-eV steps without the application of an external field. The data were then integrated over q_y, and the integrated peak intensities were calculated after subtracting the background using a cubic spline fit. These curves can be seen in Fig. 8, along with the associated values of the asymmetry ratios. (The jaggedness of the experimental asymmetry ratio curve for the third Bragg angle is due to the poor signal-to-background ratio). In Fig. 8, the asymmetry can be seen to reduce as the energy moves off resonance due to increasing penetration into the sample. For the second Bragg angle the asymmetry is close to zero off resonance at 775 eV, and for the third Bragg angle it changes from negative to positive as one moves onto resonance, although the weak signal at the third Bragg angle makes precise determination of the off-resonant asymmetry ratio impossible. This variation of the asymmetry as a function of energy or penetration depth can inform us at which value of z the handedness of the Néel component of the domain wall flips, thus allowing an estimation of the DMI [17].

Successfully modeling the experimental curves observed in this figure would confirm the proposed magnetic domain profile shown in Fig. 5(a), and would therefore represent a major advance in the field. The theoretical curves in Fig. 8 do not consider interfacial roughness, and for computational speed were performed using an ordered stripe pattern (instead of the disordered pattern used in Figs. 6 and 7). The four theoretical curves shown in Fig. 8 are for increasing levels of increase of the imaginary part of the refractive index $\Delta\beta$ due to charge scattering from the grains in the sample. We know from the observation of diffuse charge scattering in transmission geometry in previous work [6,25] that this value of $\Delta\beta$ is nonzero, and electron microscopy work on a similar sample by McVitie *et al.* [61] found an average grain size of 4 nm. Additionally, during the transmission geometry beam time leading to Ref. [6], a long-exposure normal incidence measurement was made while searching for higher-order magnetic diffraction peaks which revealed a charge scattering small-angle x-ray scattering ring corresponding to an average grain size of 8 nm. A precise measurement of losses due to diffuse scattering by the polycrystalline grains by x-ray absorption measurements in transmission geometry as a function of incidence angle and energy remains, however, to be done. It should also be noted at this point that any systematic bias in the real values of the material densities (and therefore the refractive indices) due to sample fabrication issues may also be included in this correction factor $\Delta\beta$. The fact that the measured scattering signal depends so strongly on the scattering loss is an indication that this issue will need to be resolved before a detailed characterization of the internal magnetic structure can be achieved.

As can be seen, as the degree of transmission loss due to diffuse scattering from the polycrystalline grains increases, the peak of the intensity spectra moves from 777 eV towards the experimental peak at 778 eV, but does not reach this point. The peak of the resonance is at 778 eV, and for a single layer this is where the reflection signal would be expected to be strongest. However, as one moves off resonance, the transmission increases which in the presence of a perfect multilayer stack drastically increases the reflection when measured on the Bragg angle. It could be that the local periodicity of the multilayer stack is locally imperfect, something which could be investigated in a future experiment studying the speckle from a coherent illumination experiment on a magnetically saturated sample. This could be both at high levels of photon flux with a beam stop to study high-spatial-frequency roughness, and at low flux without a beam stop for the low-spatial-frequency roughness. We suspect that it is this low-spatial-frequency background which is responsible for the weaker-than-predicted Bragg interference.

For purposes of comparison, we evaluated the scattering patterns for a perfectly smooth single magnetic interface, with domain-wall periodicity and domain-wall width equal to those on the surface layer of the sample under study. In this case, however, we assumed that the domain-wall type was either of pure Néel or pure Bloch type with these results displayed in Fig. 9.

In Fig. 9, readers should note that the maximum scattering intensity is found at 778 eV, and not at 777 eV as was seen for the multilayer simulations, further evidence that we are most likely overestimating the effects of constructive interference on the Bragg angles in our simulations. Also, we note for a pure Néel domain wall that we have an asymmetry ratio greater than 0.6 for the first two Bragg angles, whereas for a pure Bloch wall in the present scat-

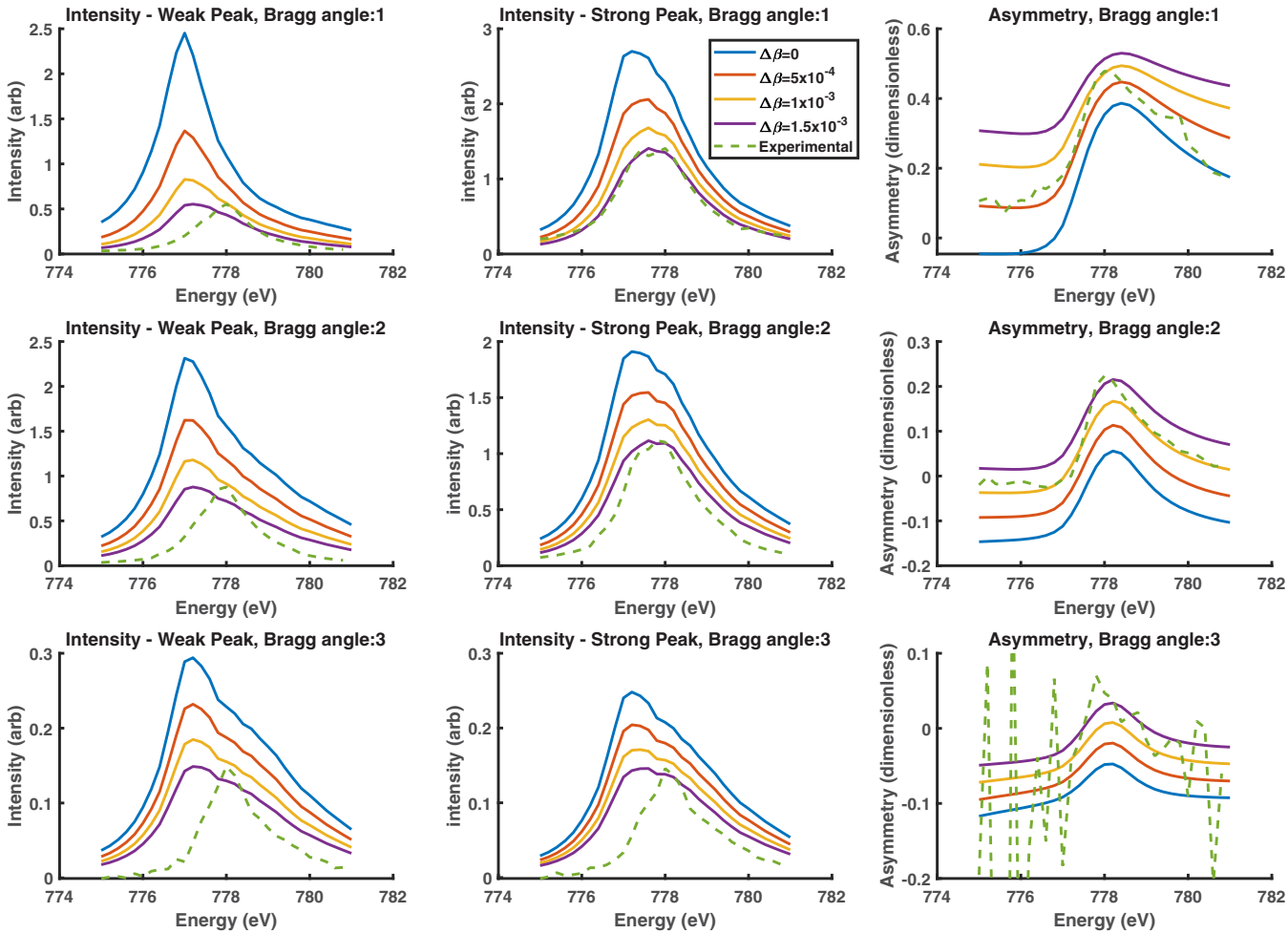

FIG. 8. Energy scans of the asymmetry ratio without roughness used in the simulations. Results for the first multilayer Bragg angle (16.8°) in the top row, the second multilayer Bragg angle (35°) in the middle row, and in the bottom row the third Bragg peak at 58.8°. Theoretical curves are shown in solid lines for different values of the polycrystalline-structure-induced change in the imaginary part of the refractive index $\Delta\beta$, and the experimental data are shown in a dashed line. The intensities of the "weak" peaks refer to the less intense scattering peak at one helicity, and the corresponding less intense peak from the opposite side as measured with the opposite helicity. The "strong" peak intensities refer to the opposite more intense scattering peaks.

tering geometry the asymmetry ratio is identically zero due to the absence of a transverse MOKE component. For this reason, the asymmetry ratios for the pure Bloch case are not shown in Fig. 9. An interesting corollary can be seen when comparing the case of the pure Néel wall and the measurement performed off the Bragg angle for the hybrid sample shown in Fig. 6. In this case, the observed asymmetry ratios are very similar, and it is imaginable that one could mistake a hybrid domain-wall sample for a pure Néel sample if only a single measurement were to be made on a suboptimally aligned sample. A simple energy scan or rocking curve measurement would, however, clear any ambiguity in that domain.

Comparing Figs. 8 and 9, we note in the case of Fig. 9 that the asymmetry in the case of the Néel walls displays only a very weak dependence on the photon energy with approximately a 0.1% variation across the energy range shown—differences unlikely to be visible in an experiment. The reason for this small energy dependence of the first-order asymmetry ratio—a quantity largely determined by the spatial interplay between the polar/longitudinal and transverse MOKE signals—is due to the fact that the different elements of the reflection coefficient matrix [Eq. (16)] have a similar energy dependence. As such, there is only a small variation of the first-order asymmetry with respect to the incident energy. As one moves off resonance, the first-order asymmetry tends towards a limit of type 0/0, becoming ever more sensitive to uncertainties caused by imperfect subtraction of the charge background—the reason for the poor quality of the experimental data for the third Bragg angle observed in Fig. 8. For a multilayer sample with a z-dependent magnetization profile as in Fig. 8, energy-dependent differences in the absorption length alter the effective magnetic morphology being probed, causing the first-order asymmetry ratio to vary notably with energy. Regarding the behavior of the magnetic scattering intensities and the asymmetry ratio of the specular peak as a function of energy (zero-order asymmetry ratio), these quantities depend directly on

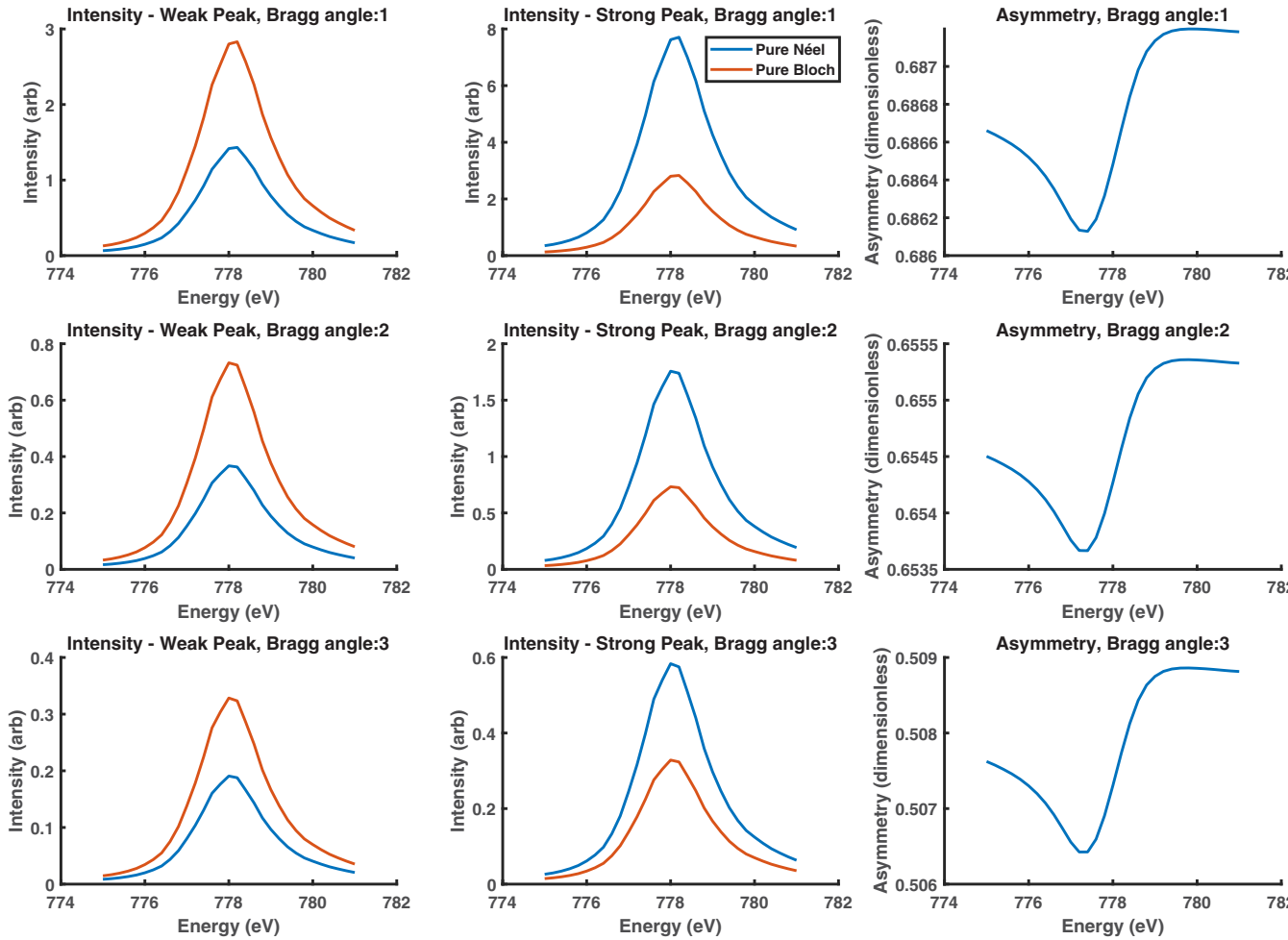

FIG. 9. Energy scans of the asymmetry ratios and scattering intensities for a hypothetical perfectly smooth interface for ordered stripe domain pattern with either pure Bloch or pure Néel domain walls. Each row represents the incidence angle equal to the first, second, or third Bragg angle corresponding to the multilayer sample studied in this paper. The intensities of the "weak" peaks refer to the less intense scattering peak at one helicity, and the corresponding less intense peak from the opposite side as measured with the opposite helicity. The "strong" peak intensities refer to the opposite more intense scattering peaks. Asymmetry ratios for the pure Bloch domain walls are identically zero due to the absence of a transverse MOKE component [2], and are therefore not shown.

f^s_{m1}, and consequently tend towards zero as one moves off resonance.

We also compare the energy scan simulation without interfacial roughness (but including an increment in the absorption due to diffuse scattering from grain boundaries $\Delta\beta = 0.001$) to one with interfacial roughness of 1 Å in Fig. 10. In this case, the simulated results shown are the mean of 100 different simulations with random roughness distributions; however, for speed we used a perfect stripe pattern as in Fig. 8. In this case, a Lorentzian roughness spectrum was used, which is relatively close to the experimental data as seen in Fig. 6. It can be seen here that the overall behavior of the (background subtracted) peak intensities for the simulated rough sample is similar to that of the ideal sample, except for an expected reduction in the scattered intensity. We note that a small systematic bias towards higher asymmetry ratios is observed for the case where roughness is present; however, the effect is small, suggesting that except in cases with very high background one is justified in not considering interference between charge and magnetic scattering when subtracting the background from experimental data. We note as well that the signal-to-background ratio is best at the first Bragg angle and gets steadily worse as we move to the second and third Bragg angles, as evidenced by the greater amount of residual noise present even after summing the results from 100 different roughness distributions. This observation of poorer signal to background is consistent with experimental results as shown in Fig. 5(e) and the case of the third Bragg angle in Fig. 8. Due to the need to sum a large quantity of diffraction patterns to obtain adequate statistics in order to generate this figure, we increased the pixel size to 8.75 nm (20 pixels per domain period), and calculated over a 60×60 array. This therefore excludes the study of coarser spatial frequencies in the roughness spectrum—a contribution which could be key for understanding why our simulations consistently overestimate the role of constructive Bragg interference at energies off resonance.

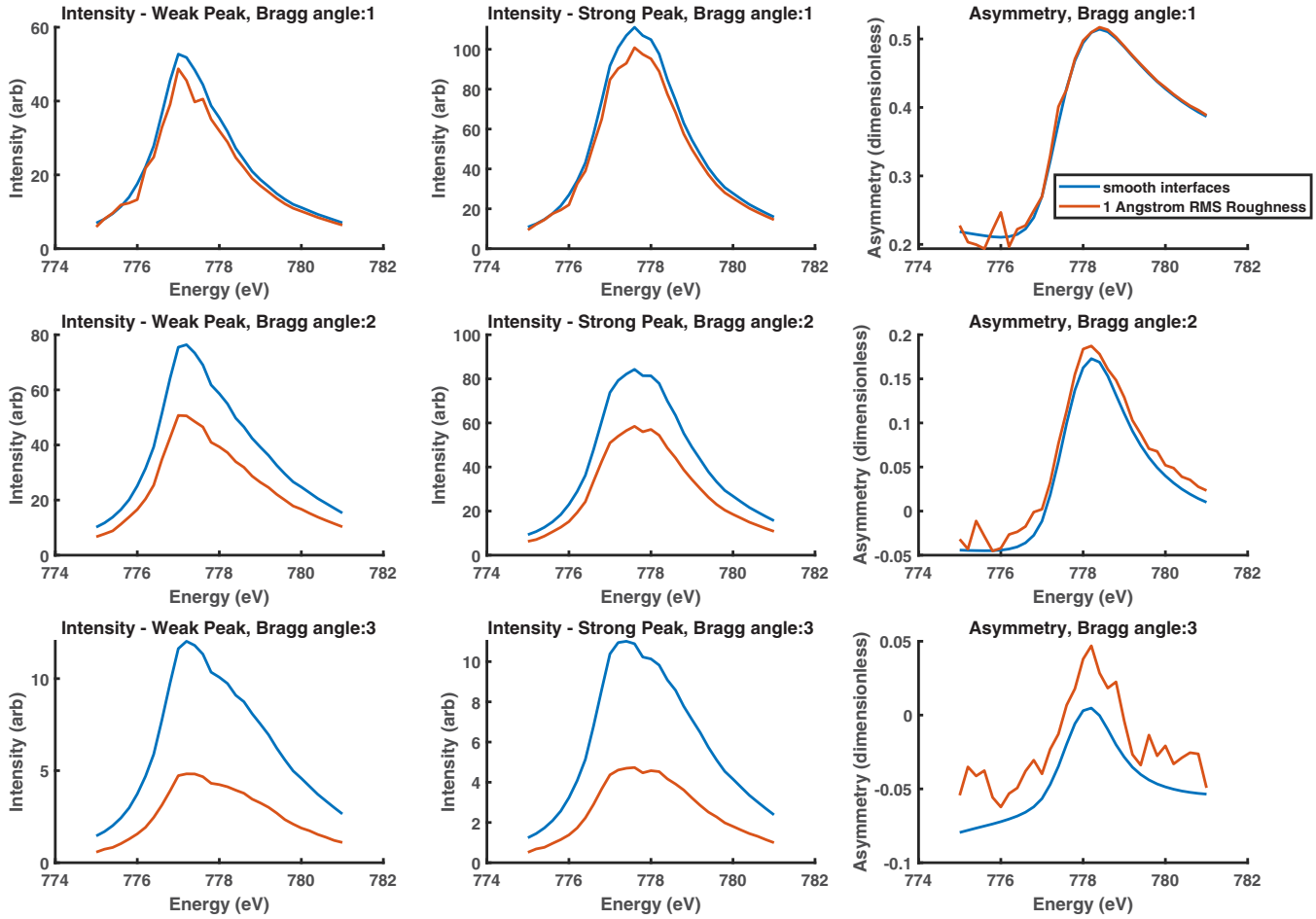

FIG. 10. Energy scans of the asymmetry ratio with 1 ÅRMS roughness used in the simulations. Results for the first multilayer Bragg angle in the top row, the second multilayer Bragg angle in the middle row, and in the bottom row the third Bragg peak. Each line represents a differing level of interfacial roughness. The intensities of the "weak" peaks refer to the less intense scattering peak at one helicity, and the corresponding less intense peak from the opposite side as measured with the opposite helicity. The "strong" peak intensities refer to the opposite more intense scattering peaks.

IV. CONCLUSION

In the course of this work we have presented a general numerical algorithm for simulating magnetic scattering from an arbitrary 3D magnetized, multilayer sample, based upon a generalization of the formalism of Zak *et al.* [9–12] in the DWBA. The algorithm was developed as a tool for the analysis of colleagues' data with the aim of creating the most general framework possible [22–24], with the further experimental tests presented in this paper devised to evaluate the algorithm's robustness. In these experiments we succeeded in achieving agreement between theory and experiment as the angle of incidence moves on and off the Bragg angle, and we also succeeded in explaining the dichroism observed in the second-order magnetic scattering peaks due to transmission through and parallel to the Bloch walls before and after the reflection event. This explanation of the dichroism of the second-order peaks is key to the work of Burgos-Parra *et al.*, where the evolution of the 3D magnetization morphology is studied as a function of applied field. Further work in the area of interfacial roughness and scattering in transmission from polycrystalline grain walls will, however, be necessary to fully explain the behavior observed as the depth penetration is varied, and will be necessary before a fully quantitative determination of magnetic structures is possible.

The long-term aim of this investigation is to extract a plausible range of magnetic structures given a set of experimental data, most likely via an iterative algorithm. There is still much work to arrive at this point, such as the optimization of an experimental protocol for the choice of measurements (energy and incidence angle), a revision of the role of micromagnetic simulations in the process, and the selection of the optimal computational algorithm for implementing the iterative process. The most significant advances presented in this present work are in our opinion the generalization of the Zak [9–12] formalism for nonspecular reflection, the addition of the DWBA allowing the study of Bloch domain walls, and the presentation of a step-by-step algorithm allowing for the scattering to be calculated from an arbitrary distribution of the magnetization. This work is not restricted to static magnetic configurations, but can be applied to time-resolved experiments, or under different temperature and external field conditions. Further benefits will also come from the highly coherent 100-nm spots available from new diffraction-limited

storage rings, which will allow the practical extension of this work to coherent scattering and speckle analysis.

ACKNOWLEDGMENTS

We thank Vincent Cross for fruitful discussions during the preparation of this work. S.F. wishes to thank Julián Milano for discussions during the primary phase of development of the algorithm. Financial support from FLAG-ERA Sograph MEM (ANR-15-GRFL-0005), funding from the Agence Nationale de la Recherche, France, under Grant Agreement No. ANR-17-CE24-0025 (TOPSKY) and Grant No. 18-CE24-0018-01 (SANTA), and the Horizon 2020 Framework Program of the European Commission under FET-Proactive Grant Agreement No. 824123 (SKYTOP) is acknowledged.

[1] J. P. Hannon, G. T. Trammell, M. Blume, and D. Gibbs, Phys. Rev. Lett. **61**, 1245 (1988).
[2] H. A. Dürr, E. Dudzik, S. S. Dhesi, J. B. Goedkoop, G. van der Laan, M. Belakhovsky, C. Mocuta, A. Marty, and Y. Samson, Science **284**, 2166 (1999).
[3] G. Beutier, G. van der Laan, K. Chesnel, A. Marty, M. Belakhovsky, S. P. Collins, E. Dudzik, J.-C. Toussaint, and B. Gilles, Phys. Rev. B **71**, 184436 (2005).
[4] J.-Y. Chauleau, W. Legrand, N. Reyren, D. Maccariello, S. Collin, H. Popescu, K. Bouzehouane, V. Cros, N. Jaouen, and A. Fert, Phys. Rev. Lett. **120**, 037202 (2018).
[5] B. Pfau, S. Schaffert, L. Müller, C. Gutt, A. Al-Shemmary, F. Büttner, R. Delaunay, S. Düsterer, S. Flewett, R. Frömter *et al.*, Nat. Commun. **3**, 1100 (2012).
[6] S. Flewett, T. J. A. Mori, A. Ovalle, S. Oyarzún, A. Ibáñez, S. Michea, J. Escrig, and J. Denardin, Sci. Rep. **9**, 14823 (2019).
[7] J. Hill and D. McMorrow, Acta Crystallogr. Sect. A **52**, 236 (1996).
[8] J. M. Tonnerre, L. Sève, D. Raoux, G. Soullié, B. Rodmacq, and P. Wolfers, Phys. Rev. Lett. **75**, 740 (1995).
[9] J. Zak, E. R. Moog, C. Liu, and S. D. Bader, J. Appl. Phys. **68**, 4203 (1990).
[10] J. Zak, E. R. Moog, C. Liu, and S. D. Bader, J. Magn. Magn. Mater. **89**, 107 (1990).
[11] J. Zak, E. R. Moog, C. Liu, and S. D. Bader, Phys. Rev. B **43**, 6423 (1991).
[12] J. Zak, E. R. Moog, C. Liu, and S. D. Bader, Phys. Rev. B **46**, 5883(E) (1992).
[13] M. J. Donahue and D. G. Porter, *OOMMF User's Guide*, version 1.0 (National Institute of Standards and Technology, Gaithersburg, MD, 1999), http://math.nist.gov/oommf/.
[14] A. Vansteenkiste, J. Leliaert, M. Dvornik, M. Helsen, F. Garcia-Sanchez, and B. Van Waeyenberge, AIP Adv. **4**, 107133 (2014).
[15] J.-Y. Chauleau, T. Chirac, S. Fusil, V. Garcia, W. Akhtar, J. Tranchida, P. Thibaudeau, I. Gross, C. Blouzon, A. Finco *et al.*, Nat. Mater. **19**, 386 (2020).
[16] S. Fin, R. Tomasello, D. Bisero, M. Marangolo, M. Sacchi, H. Popescu, M. Eddrief, C. Hepburn, G. Finocchio, M. Carpentieri *et al.*, Phys. Rev. B **92**, 224411 (2015).
[17] W. Legrand, J.-Y. Chauleau, D. Maccariello, N. Reyren, S. Collin, K. Bouzehouane, N. Jaouen, V. Cros, and A. Fert, Sci. Adv. **4**, eaat0415 (2018).
[18] S. Zhang, G. van der Laan, J. Müller, L. Heinen, M. Garst, A. Bauer, H. Berger, C. Pfleiderer, and T. Hesjedal, Proc. Natl. Acad. Sci. U.S.A. **115**, 6386 (2018).
[19] W. Li, I. Bykova, S. Zhang, G. Yu, R. Tomasello, M. Carpentieri, Y. Liu, Y. Guang, J. Gräfe, M. Weigand *et al.*, Adv. Mater. **31**, 1807683 (2019).
[20] S. L. Zhang, G. van der Laan, W. W. Wang, A. A. Haghighirad, and T. Hesjedal, Phys. Rev. Lett. **120**, 227202 (2018).
[21] J. Díaz, P. Gargiani, C. Quirós, C. Redondo, R. Morales, L. M. Álvarez-Prado, J. I. Martín, A. Scholl, S. Ferrer, M. Vélez *et al.*, Nanotechnology **31**, 025702 (2019).
[22] E. Burgos-Parra, S. Flewett, Y. Sassi, W. Legrand, F. Ajejas, C. Leveille, P. Gargiani, M. Valdivares, N. Reyren, V. Cros *et al.* (unpublished).
[23] B. Pianciola, S. Flewett, E. De Biasi, C. Hepburn, L. Lounis, M. Vásquez-Mansilla, M. Granada, M. Barturen, M. Eddrief, M. Sacchi *et al.*, Phys. Rev. B **102**, 054438 (2020).
[24] C. Léveille, S. Flewett, Y. Sassi, M. Garrido, N. Jaouen, N. Reyren, W. Legrand, F. Ajejas, and V. Cros (unpublished).
[25] S. Flewett, D. Mishra, T. J. A. Mori, C. M. Günther, J. C. Denardin, S. Oyarzún, S. Michea, D. Engel, M. Fohler, T. C. R. Rocha *et al.*, Phys. Rev. B **95**, 094430 (2017).
[26] S. Zhang, D. M. Burn, N. Jaouen, J.-Y. Chauleau, A. A. Haghighirad, Y. Liu, W. Wang, G. van der Laan, and T. Hesjedal, Nano Lett. **20**, 1428 (2020).
[27] R. G. Newton, Am. J. Phys. **44**, 639 (1976).
[28] G. van der Laan, C. R. Phys. **9**, 570 (2008).
[29] S. Macke and E. Goering, J. Phys.: Condens. Matter **26**, 363201 (2014).
[30] M. Elzo, E. Jal, O. Bunau, S. Grenier, Y. Joly, A. Ramos, H. Tolentino, J. Tonnerre, and N. Jaouen, J. Magn. Magn. Mater. **324**, 105 (2012).
[31] L. G. Parratt, Phys. Rev. **95**, 359 (1954).
[32] M. Mansuripur, J. Appl. Phys. **67**, 6466 (1990).
[33] A. Bourzami, O. Lenoble, C. Féry, J. F. Bobo, and M. Piecuch, Phys. Rev. B **59**, 11489 (1999).
[34] Z. Q. Qiu and S. D. Bader, Rev. Sci. Instrum. **71**, 1243 (2000).
[35] J. M. Tonnerre, M. De Santis, S. Grenier, H. C. N. Tolentino, V. Langlais, E. Bontempi, M. García-Fernández, and U. Staub, Phys. Rev. Lett. **100**, 157202 (2008).
[36] J.-M. Tonnerre, E. Jal, E. Bontempi, N. Jaouen, M. Elzo, S. Grenier, H. L. Meyerheim, and M. Przybylski, Eur. Phys. J.: Spec. Top. **208**, 177 (2012).
[37] H.-C. Mertins, S. Valencia, D. Abramsohn, A. Gaupp, W. Gudat, and P. M. Oppeneer, Phys. Rev. B **69**, 064407 (2004).
[38] T. Kuschel, C. Klewe, J.-M. Schmalhorst, F. Bertram, O. Kuschel, T. Schemme, J. Wollschläger, S. Francoual, J. Strempfer, A. Gupta *et al.*, Phys. Rev. Lett. **115**, 097401 (2015).
[39] C. Klewe, T. Kuschel, J.-M. Schmalhorst, F. Bertram, O. Kuschel, J. Wollschläger, J. Strempfer, M. Meinert, and G. Reiss, Phys. Rev. B **93**, 214440 (2016).
[40] S. Macke, A. Radi, J. E. Hamann-Borrero, A. Verna, M. Bluschke, S. Brück, E. Goering, R. Sutarto, F. He, G. Cristiani, M. Wu, E. Benckiser, H.-U. Habermeier, G. Logvenov, N.

Gauquelin, G. A. Botton, A. P. Kajdos, S. Stemmer, G. A. Sawatzky, M. W. Haverkort, B. Keimer, and V. Hinkov, Adv. Mater. **26**, 6554 (2014).

[41] M. Zwiebler, J. E. Hamann-Borrero, M. Vafaee, P. Komissinskiy, S. Macke, R. Sutarto, F. He, B. Büchner, G. A. Sawatzky, L. Alff *et al.*, New J. Phys. **17**, 083046 (2015).

[42] S. Valencia, A. Gaupp, W. Gudat, L. Abad, L. Balcells, and B. Martinez, J. Appl. Phys. **104**, 023903 (2008).

[43] F. D'Orazio, F. Giammaria, and F. Lucari, J. Magn. Magn. Mater. **133**, 419 (1994).

[44] F. D'Orazio, F. Giammaria, and F. Lucari, J. Magn. Magn. Mater. **140-144**, 2123 (1995).

[45] G. H. Vineyard, Phys. Rev. B **26**, 4146 (1982).

[46] B. Henke, E. Gullikson, and J. Davis, At. Data Nucl. Data Tables **54**, 181 (1993).

[47] N.-T. D. Loh, S. Eisebitt, S. Flewett, and V. Elser, Phys. Rev. E **82**, 061128 (2010).

[48] S. A. Kovalenko, Semicond. Phys. Quantum Electron. Optoelectron. **4**, 214 (2001).

[49] D. R. Lee, S. K. Sinha, D. Haskel, Y. Choi, J. C. Lang, S. A. Stepanov, and G. Srajer, Phys. Rev. B **68**, 224409 (2003).

[50] D. R. Lee, S. K. Sinha, C. S. Nelson, J. C. Lang, C. T. Venkataraman, G. Srajer, and R. M. Osgood, Phys. Rev. B **68**, 224410 (2003).

[51] A. Scherz, W. F. Schlotter, K. Chen, R. Rick, J. Stöhr, J. Lüning, I. McNulty, C. Günther, F. Radu, W. Eberhardt *et al.*, Phys. Rev. B **76**, 214410 (2007).

[52] S. Eisebitt, J. Lüning, W. F. Schlotter, M. Lörgen, O. Hellwig, W. Eberhardt, and J. Stöhr, Nature **432**, 885 (2004).

[53] C. Donnelly, M. Guizar-Sicairos, V. Scagnoli, S. Gliga, M. Holler, J. Raabe, and L. J. Heyderman, Nature **547**, 328 (2017).

[54] P. Li and A. Maiden, Sci. Rep. **8**, 2049 (2018).

[55] S. Flewett, H. M. Quiney, C. Q. Tran, and K. A. Nugent, Opt. Lett. **34**, 2198 (2009).

[56] N. Jaouen, J.-M. Tonnerre, G. Kapoujian, P. Taunier, J.-P. Roux, D. Raoux, and F. Sirotti, J. Synchrotron Radiat. **11**, 353 (2004).

[57] M. Sacchi, N. Jaouen, H. Popescu, R. Gaudemer, J. M. Tonnerre, S. G. Chiuzbaian, C. F. Hague, A. Delmotte, J. M. Dubuisson, G. Cauchon *et al.*, J. Phys.: Conf. Ser. **425**, 072018 (2013).

[58] R. Soucaille, M. Belmeguenai, J. Torrejon, J.-V. Kim, T. Devolder, Y. Roussigné, S.-M. Chérif, A. A. Stashkevich, M. Hayashi, and J.-P. Adam, Phys. Rev. B **94**, 104431 (2016).

[59] A. K. Chaurasiya, C. Banerjee, S. Pan, S. Sahoo, S. Choudhury, J. Sinha, and A. Barman, Sci. Rep. **6**, 32592 (2016).

[60] P. M. Shepley, H. Tunnicliffe, K. Shahbazi, G. Burnell, and T. A. Moore, Phys. Rev. B **97**, 134417 (2018).

[61] S. McVitie, S. Hughes, K. Fallon, S. McFadzean, D. McGrouther, M. Krajnak, W. Legrand, D. Maccariello, S. Collin, K. Garcia *et al.*, Sci. Rep. **8**, 5703 (2018).